MRS Communications
© The Author(s), 2026
https://doi.org/10.1557/s43579-026-01056-0

MRS Communications

Research Letter

Exploring defect-induced deformation in polymeric microlattices using laboratory-based X-ray nanotomography

Rafaela Debastiani, Institute of Nanotechnology, Karlsruhe Institute of Technology, Hermann-von-Helmholtz-Platz 1, 76344 Eggenstein-Leopoldshafen, Germany; Karlsruhe Nano Micro Facility (KNMFi), Karlsruhe Institute of Technology (KIT), Hermann-von-Helmholtz-Platz 1, 76344 Eggenstein-Leopoldshafen, Germany; Helmholtz Institute Freiberg for Resource Technology, Helmholtz-Zentrum Dresden-Rossendorf, Chemnitzer Straße 40, 09599 Freiberg, Germany

Chantal M. Kurpiers, Institute for Applied Materials (IAM), Karlsruhe Institute of Technology (KIT), Kaiserstr. 12, 76131 Karlsruhe, Germany

Santiago Gomez Melo, Johannes Blumberg, and Ulrich S. Schwarz, Institute for Theoretical Physics, Heidelberg University, Philosophenweg 16, 69120 Heidelberg, Germany; Bioquant, Heidelberg University, Im Neuenheimer Feld 267, 69120 Heidelberg, Germany

Peter Gumbsch, Institute of Nanotechnology, Karlsruhe Institute of Technology, Hermann-von-Helmholtz-Platz 1, 76344 Eggenstein-Leopoldshafen, Germany; Fraunhofer Institute for Mechanics of Materials IWM, 79108 Freiburg, Germany

Ruth Schwaiger, Institute of Energy Materials and Devices—Structure and Function of Materials (IMD-1), Forschungszentrum Jülich, 52425 Jülich, Germany; Faculty 5, Chair of Energy Engineering Materials, RWTH Aachen University, 52056 Aachen, Germany

Address all correspondence to Ruth Schwaiger at **r.schwaiger@fz-juelich.de**

(Received 23 January 2026; accepted 16 September 2026)

Abstract

Defects introduced during additive manufacturing strongly influence the mechanical response of architected materials, yet their evolution under load is difficult to resolve at the micrometer scale. Laboratory-based X-ray nanotomography (nanoCT) at 128 nm voxel size was used here to image tetrahedral polymeric microlattices, printed defect-free and with three omitted beams, during *in situ* compression. Image registration yielded three-dimensional displacement fields, and finite element simulations reproduced the measured behavior. Displacement was markedly reduced at the defect and recovered in neighboring unit cells, with an accompanying stiffness reduction. Laboratory nanoCT thus provides a practical route to validate models of architected materials.

Introduction

Mechanical metamaterials explore material–property spaces beyond conventional limits, achieving unprecedented properties at low densities[1,2] by integrating advanced manufacturing techniques and post-processing methods. Mechanical metamaterials also offer insights into biological systems, where self-assembly processes enable the same material to exhibit distinct mechanical properties by varying geometry (e.g., branched networks versus bundles of the structural protein actin).[3] Prior research has emphasized the tunability of mechanical behavior through material modifications or geometric adjustments. For example, polymeric structures show variations in strength and stiffness due to changes in printing parameters, which alter material crosslinking.[4] Geometric adjustments include modifying beam and node shapes[5] or incorporating reinforced structural elements.[6,7] Strategically placed defects further tailor mechanical performance. Studies have analyzed how the size and position of designed vacancies in lattice structures influence buckling and mechanical properties by the removal of beam elements.[8–10] Gross et al.[9] demonstrated changes in effective properties based on vacancy size, fraction, and location, while Vangelatos et al.[8] used finite element modeling (FEM) to evaluate the energy absorption in lattices with designed vacancies. Additionally, the effects of pores and material heterogeneity have been explored using experimental and computational methods.[11]

To study the influence of geometry and material variations on mechanical properties of metamaterials, researchers have employed experimental techniques, such as *in situ* scanning electron microscopy testing[12,13] complemented by computational approaches for validating results and conducting parametric studies.[6,8] Advanced analysis methods are critical for complex materials at the nano- and micrometer scales. Innovations in *in situ* X-ray tomography and nanotomography have enhanced understanding of internal structure evolution during mechanical testing.[14–16] These methods, combined with digital image processing, enable detailed analysis of localized displacement and strain concentrations in three-dimensional datasets.[15,17] Such techniques have been applied to trabecular bone, foam materials, and millimeter-scale lattices,[18–21] though primarily to high-density materials at voxel sizes of tens of micrometers, using both synchrotron and laboratory sources. However, laboratory-based X-ray tomographic investigations of micrometer-scale lattice structures remain scarce. Debastiani et al.[22] highlighted the challenges of *in situ* mechanical testing for low-contrast polymeric microlattices using lab-based X-ray tomography.

Rafaela Debastiani, Chantal M. Kurpiers, and Santiago Gomez Melo have contributed equally to the manuscript.

In this work, laboratory-based X-ray nanotomography (nanoCT) was employed to characterize the 3D morphology of defects in polymeric microlattices. *In situ* compression tests allowed the influence of defects on mechanical behavior to be assessed. Displacement fields within tetrahedral lattice structures were then visualized using 3D image processing and registration. These findings were validated through finite element simulations, providing deeper insights into the role of defects in these architected materials.

Materials and methods

Sample preparation and structural characterization

Polymeric microlattices with a tetrahedral geometry and strut length of 10 µm [Fig. 1(a)] were fabricated using 3D direct laser writing (3D-DLW) via a Photonic Professional GT2 system (Nanoscribe GmbH, Eggenstein-Leopoldshafen, Germany). Both defect-free lattices and those with intentionally introduced beam defects were printed.

The structures were fabricated using IP-Dip resin (Nanoscribe GmbH, Eggenstein-Leopoldshafen, Germany) with a laser power of 6.7 mW, a printing speed of 3000 µm/s, and hatching/slicing distances of 200 nm. The tetrahedral geometry was designed in MATLAB (The MathWorks Inc., Natick, MA, USA) with a beam length L of 10 µm, resulting in an overall model height H of 36.5 µm and diameter D of 61.0 µm [Fig. 1(a)]. The beam diameter was defined using the diameter-to-length ratio of inclined beams $\frac{d_{inclined}}{L}$ at a value of 0.19 (Fig. S1). Printing with the layer-by-layer galvo scanning mode necessitated distinct strategies for fabricating inclined and horizontal beams. The oval shape of the voxel resulted in beams with different varying widths and heights. Inclined beams were produced by printing concentric circles outward from the center, illustrated in Fig. S2. As shown in Fig. 1(b), the diameters of inclined beams $d_{inclined}$ were measured perpendicular to the beam axis, yielding two distinct values: $d_{inclined,1}$ and $d_{inclined,2}$ (Fig. S1, Fig. S2). Horizontal beams, created by adjacent voxel lines, had their height and width measured as $d_{horizontal}$ [Fig. 1(b)].

For defect studies, a microlattice was printed with three inclined beams intentionally omitted [red beams in Fig. 1(b)] between the third and fourth horizontal planes [Fig. 1(a)]. To facilitate visibility during nanoCT imaging and prevent manufacturing-induced defects, microlattices were printed atop 500-µm-diameter titanium sample holders on printed small circular pedestals [Fig. 1(c) and (d)].

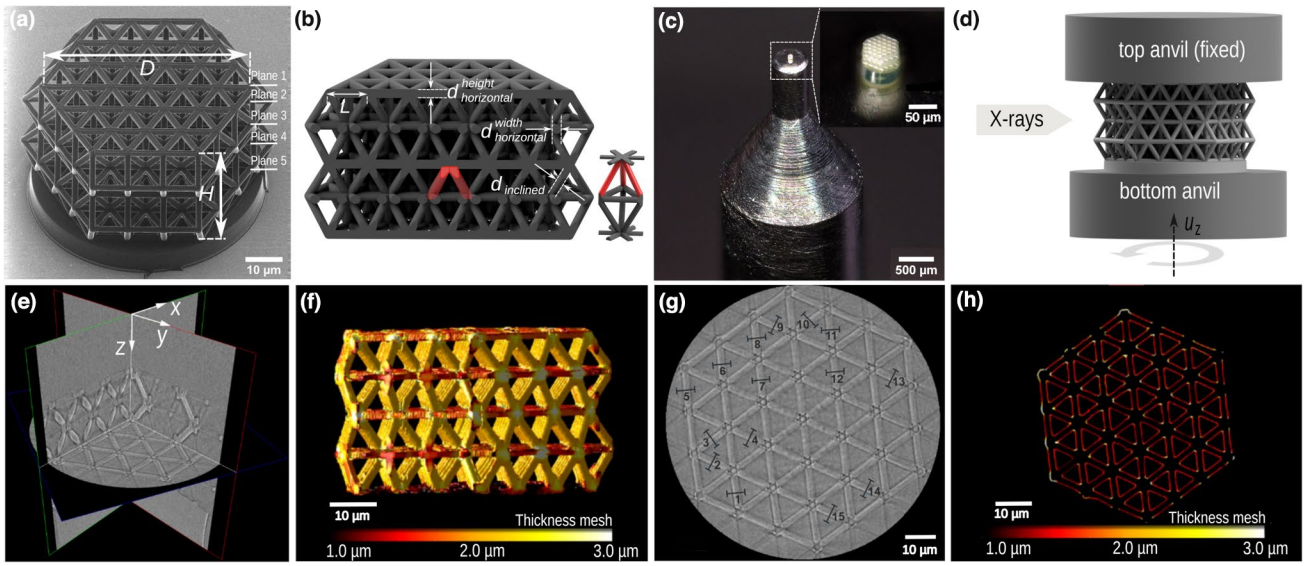


Figure 1. (a) Helium ion microscopy micrograph of the printed tetrahedral structure with height H, diameter D, and horizontal planes 1 through 5. (b) CAD model of a cross section of the tetrahedral structure and its unit cell, indicating the beam length L and the diameters of inclined ($d_{inclined}$) and horizontal ($d_{horizontal}$) beams. Omitted inclined beams (highlighted in red) are located between the third and fourth horizontal planes at the center of the lattice. (c) NanoCT sample holder with the tetrahedral lattice structure printed on top with the inset showing the tetrahedral structure on the polymer pedestal printed on the pin. (d) Schematic of the experimental setup for nanoCT compression tests. During testing, the sample holder moves upward, compressing the sample against a fixed diamond anvil, while scans are performed over a 140° rotation. (e) Multiplanar views (*xy*, *xz* and *yz* planes) showing the microlattice structure of the defect-free lattice. (f) Segmented 3D model of the tetrahedral structure with an overlaid thickness mesh. Color coding indicates thickness, ranging from dark red (thinnest) to white (thickest). (g) Top view (*xy* plane) highlighting the measurement positions of $d^{width}_{horizontal}$ within the third horizontal plane. (h) *xy* view of the thickness mesh, illustrating the uniform beam diameters of the horizontal beams in plane 3 (outlined in red).

X-ray nanotomography

The 3D structural and *in situ* mechanical characterization were performed using the lab-based X-ray microscope Xradia 810 Ultra (Carl Zeiss AG, Oberkochen, Germany). Samples were scanned in both absorption and Zernike phase contrast modes using a quasi-monochromatic X-ray beam from a Cr anode (5.4 keV), achieving a pixel size of 128 nm within a 65 µm field of view. For structural characterization, 901 projections were acquired over 180° with an acquisition time of 20–30 s per projection.

The term nanotomography refers to the resolution regime of the imaging technique rather than to the dimensions of the specimen. With a voxel size of 128 nm and a spatial resolution of approximately 300 nm, the instrument resolves displacements well below the beam diameters of 1.7–2.3 µm reported here. This resolution is a prerequisite for the present study: the displacement differences distinguishing defective from defect-free lattices are of the order of a few hundred nanometers, whereas laboratory tomography of architected lattices is typically performed at voxel sizes of tens of micrometers on millimeter-scale specimens,[21] where differences of this magnitude would not be separable from noise.

Two samples, one defect-free and one with a deliberately introduced defect, underwent *in situ* nanoCT testing. Compression tests were performed using the nanoCT loading stage,[22] where the sample holder acted as the bottom anvil, pressing the samples against a top anvil to achieve specified displacements [Fig. 1(d)]. Due to geometric constraints of the loading stage, the 901 projections were acquired over 140°, which may result in incomplete reconstruction due to uneven X-ray illumination. This issue can be mitigated by orienting the sample on the pin to ensure more uniform X-ray exposure, enabling more accurate reconstruction.[22]

Incremental *in situ* compression tests were conducted in three steps, corresponding to forces of 8 mN, 12 mN, and 15 mN, measured with a force gauge attached to the sample holder. For the defect-free and defective microlattices, these forces resulted in displacements of 1.3, 3.7, and 7.2 µm, and 1.1, 3.6, and 7.2 µm, respectively. After each displacement step, the samples were allowed sufficient relaxation time to prevent image blur. During the relaxation period (approximately 10 h), 2D projections were acquired to monitor sample relaxation (Video S3, Fig. S4). Following this period, scans in absorption and Zernike phase contrast modes were conducted before proceeding to the next compression step.

Projections were reconstructed into 3D structures using the Zeiss Scout and Scan™ Control System Reconstructor (version 13.08), which uses a filtered back projection (FBP) algorithm. Image analysis was conducted using ORS Dragonfly software (Object Research Systems (ORS) Inc., Montreal, Canada), employing the UNet deep learning algorithm for segmentation, followed by manual corrections to address inaccuracies in the segmentation.

Measurements of structural dimensions, such as beam sizes and digital volume correlation, were performed on both phase contrast and segmented data. Lattice uniformity was assessed by generating thickness meshes from the segmented data. These color-coded meshes represent local wall thicknesses, calculated as the diameter of a sphere that fits within each boundary point. This method provided a detailed evaluation of the structural consistency of the lattices.

Image registration and finite element simulations

To gain a detailed understanding of the deformation behavior of polymeric lattice structures, 3D image data acquired in phase contrast mode during *in situ* compression tests were analyzed rigorously. Each compression step was evaluated individually. The 3D displacement field between two deformation states of the microlattices was determined using the open-source software *elastix*.[23] Originally developed for medical image processing, *elastix* supports a wide range of transformation models and cost functions. In this study, the B-spline representation was employed with normalized correlation as the cost function. The strain tensor was computed using custom-developed code, following the direct method,[24] which involves calculating derivatives of the 3D displacement field.

To validate the experimental results, they were compared to linear elasticity finite element (FE) simulations performed using the open-source FE solver *FEniCS*.[25] The structural model was first created in Abaqus/CAE (Version 2023, Dassault Systèmes, Vélizy-Villacoublay, France), with beam diameter-to-length $\frac{d_{inclined}}{L}$ of 0.23, as observed by both SEM and nanoCT imaging. The model was then meshed using the open-source meshing software *Gmsh*[26] with a maximum element size of 0.5 µm.

Mechanical equilibrium equations were solved with Dirichlet boundary conditions, specifying displacements at the structure's top and bottom. The bottom displacement corresponded to the compression step imposed by the sample holder. To account for the structure's tilting, a linearly increasing displacement u_z along the x-coordinate was prescribed at the top. The displacement followed the form $u_z = A\frac{x - x_{min}}{x_{max} - x_{min}}$. Here, x_{min} and x_{max} are the minimum and maximum x-coordinates, respectively, and the constant A assumes a value of 2 µm. This displacement was applied only in the z-direction, i.e., $u_x = u_y = 0$. The strain was subsequently calculated from the resulting displacement solution. The image processing, strain computation, and FE simulations were automated to allow batch processing.

Results

Achieving a voxel size of 128 nm in both phase and absorption contrast through lab-based nanoCT enabled, for the first time, a precise three-dimensional structural characterization of tetrahedral microlattices. This revealed critical details, including structural dimensions (Fig. 1), printing variability (Fig. S1), and undesired voids inside the samples (Fig. S3).

Structural characterization

By virtually cutting through reconstructed data [Fig. 1(e)], the structural elements can be investigated. A complete 3D representation of the defective lattice is available in Video S1. The segmented 3D model [Fig. 1(f)] visualizes thickness variations across the structure. The individual beam diameters were measured in the different planes of the structure [Fig. 1(g)] with consistent thickness observed for horizontal beams, for example in plane 3 [Fig. 1(h), red contour].

Key structural measurements at three locations within the defect-free microlattice yielded an overall height H=33.90 ± 0.65 μm, diameter D=56.90 ± 0.25 μm, and beam length L=9.6 ± 0.1 μm. The relative density was calculated directly from the segmented 3D data, yielding 20.2 ± 0.3% for the defect-free lattice. This contrasts with prior estimations using CAD models[27] or destructive techniques such as time-consuming focused ion beam milling,[5] which yielded lower values, i.e., 17.4%, due to assumptions of ideal beam geometry and roundness of the beams.

Homogeneity of the lattice was assessed across different planes. Planes 1 and 3 demonstrated uniform beam dimensions [Fig. 1(f), Table S1], while planes 2 and 4 exhibited minor variations of up to five pixels (~600 nm) in width, i.e., in the *xy* plane (Fig. S1). Despite these deviations, the beam diameters across all planes were generally consistent in height, i.e., in the *xz* and *yz* planes. The thickness meshes [Fig. 1(f) and Video S2] further emphasized the uniformity of inclined and horizontal beams, suggesting robust structural integrity.

Deformation behavior under compression

Figure 2 presents cross-sectional views of the defect-free and defective lattices at various compression steps. In step I, both lattices deformed uniformly, with no discernible effects from the defect. A slight tilt (~2°) of the anvil introduced off-axis loading, visible as localized deformation in the upper regions. By step II, the inclined beams near the defect in the defective sample exhibited noticeable bending, a behavior absent in the defect-free lattice. At step III, deformation localized further around the defect, particularly in inclined beams above the vacancy. The defect-free tetrahedral lattice exhibited homogeneous deformation in all planes.

Measurements of the distance between horizontal planes 3 and 4 [Fig. 2(b)] confirmed that deformation was non-uniform in the sample with defect, with significantly greater deformation at node 0 (center of defect) and neighboring nodes (−1 and +1) compared to the defect-free lattice. The missing beams introduced additional degrees of freedom, resulting in increased motion.

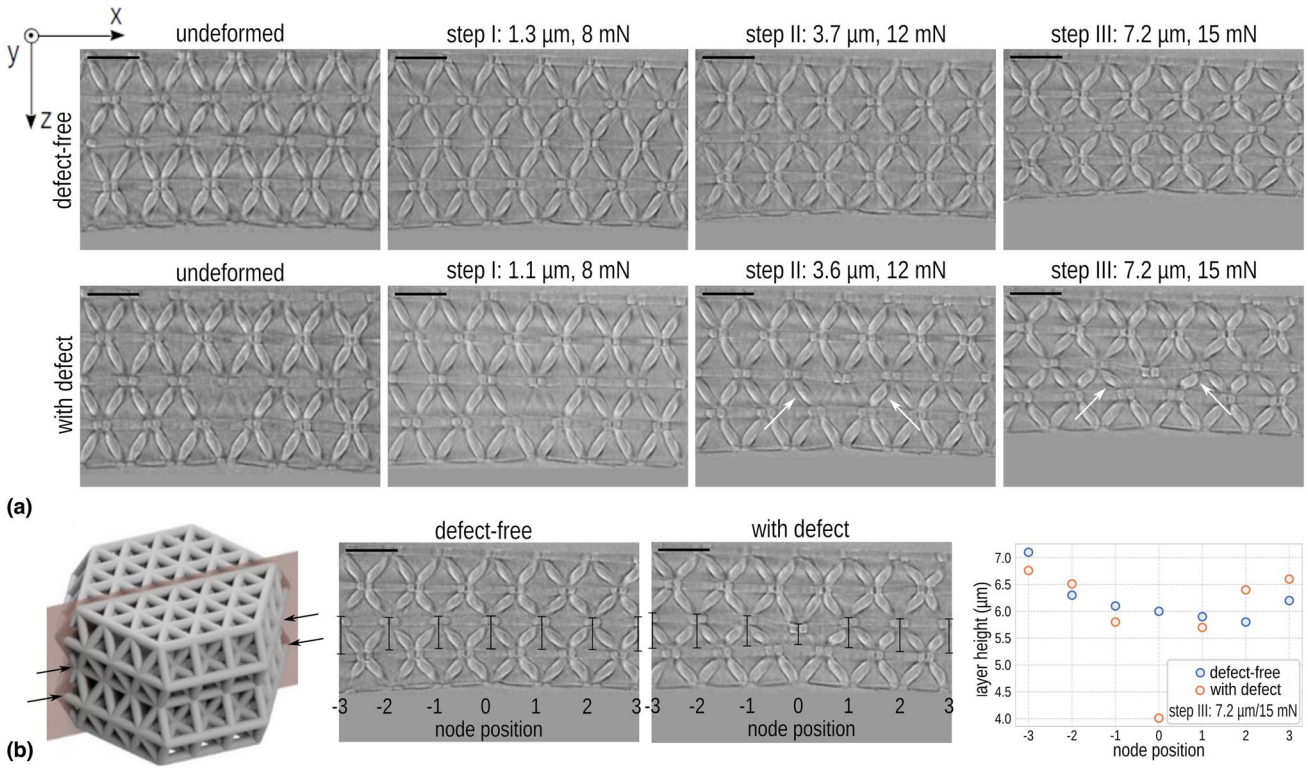


Figure 2. Analysis of tetrahedral microlattice deformation using nanoCT: (a) 2D cross-sectional slices of the defect-free and defective tetrahedral structures in their undeformed state and at three displacement steps (I, II, and III). The force applied at each step is indicated. Values above the images represent the overall lattice deformation during compression. In steps II and III, bending of the inclined beams near the defect can be seen (marked by arrows). (b) The height between horizontal planes 3 and 4 was measured from 2D scans at displacement step III. The 3D model shows the location of cross sections and planes analyzed. At each node, three measurements were taken, with results presented in the graph on the right. Scale bars in (a) and (b) refer to 10 µm.

Figure 3(a) shows the displacement distribution (*z*-direction) obtained through automated image registration, with good agreement with manual measurements (Fig. S6). Differences between the two methods were within the resolution limit of the nanoCT (~300 nm), with a maximum deviation of ~600 nm. Strain fields calculated using the direct method (Fig. S5) were unreliable due to resolution challenges; thus, FE simulations (Fig. 4) were employed, providing consistent and precise insights into strain localization.

Displacement and strain analysis

FE simulations corroborated experimental observations, demonstrating uniform displacement in the *z*-direction in step I for both lattices (Fig. 3), with minor deviations (~200 nm, i.e., 1–2 pixels in the X-ray image) attributed to experimental uncertainty. Differences became more pronounced in step II, where inclined beams above the defect showed reduced displacement compared to neighboring beams. For instance, in step II, the central node displacement was 1.3 µm in the defective lattice versus 2.7 µm in the defect-free lattice, as validated by both experiments and simulations.

The FE-calculated strain distributions (Fig. 4) revealed localized strain reduction around the defect node, with near-zero strain at this location in both steps I and II. By contrast, the defect-free lattice exhibited strains of −4% (step I) and −10% (step II) at the central node. Increased strain concentration was

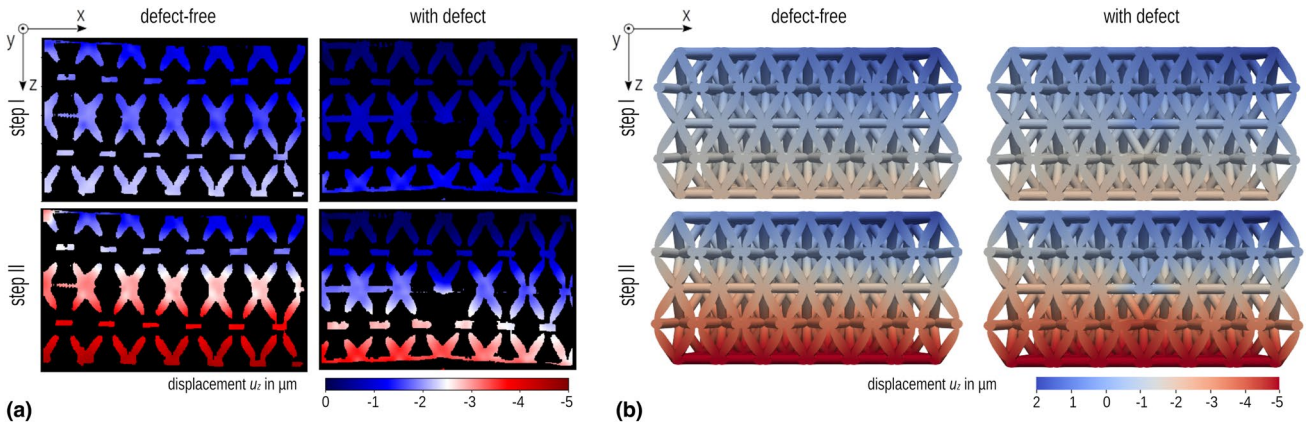


Figure 3. Displacement in *z*-direction across the cross section of defect-free and defective samples during the first two displacement steps (I, II). (a) Displacement distributions obtained from image registration. (b) Displacement distributions predicted by FE simulations.

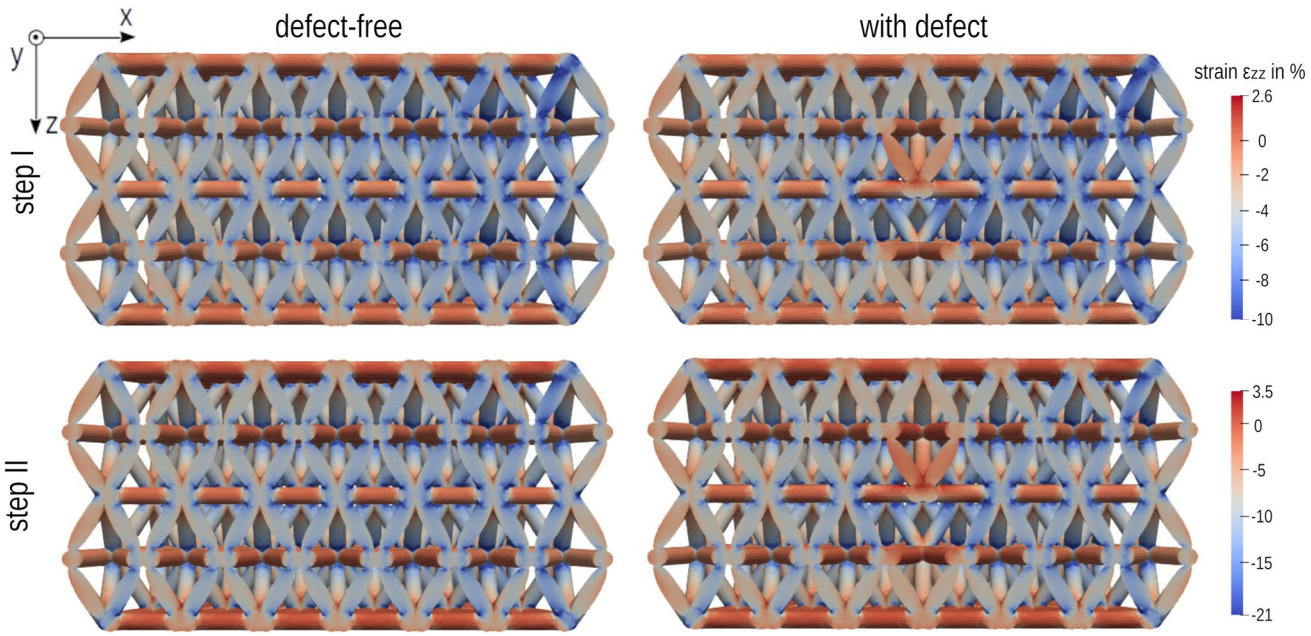


Figure 4. Strain ε_{zz} results of FE simulations in the cross section of defect-free and defective samples. Strain distributions are presented for the first and second displacement steps (I, II).

observed in corner nodes, consistent with stress accumulation in thin beam regions.

From the nanoCT images, a notable difference between the two lattices can be seen after compression step II [Fig. 3(a), right side]. Specifically, the inclined beams above the defect exhibit smaller displacements compared to their neighboring beams within the same plane. Although FE simulations had predicted this behavior during step I, it was not until displacement step II that the differences became pronounced enough to be captured by the image reconstruction algorithm.

The reduced displacement of the inclined beams above the defect, as shown in Fig. 2, aligns well with the FE simulation results. The most significant observation is the localized reduction in the displacement field magnitude at the defect site (Fig. 3). This reduction is attributed to the absence of counterforce from the missing beams. For displacement step II, the central node in the defective sample displays a displacement of 1.3 µm, compared to 2.7 µm in the defect-free counterpart. Similarly, the FE simulations predict corresponding displacements of 1.2 and 2.5 µm, demonstrating good agreement between experimental data and simulations.

Strain distribution and defect effects

Figure 4 shows FE-simulated strain (ε_{zz}) distributions for both lattice types. The strain field increases with increasing x, with leftmost inclined beams experiencing lower strains (−2% at step I, −5% at step II) compared to rightmost beams (−10% at step I, −20% at step II). Defects reduce strain near the vacancy, where strain at the central node approaches zero in both loading steps. By contrast, the defect-free lattice shows strains of −4% (step I) and −10% (step II) at the central node. Elevated strain areas were observed at node corners in all cases.

Discussion

The laboratory-based nanoCT technique was employed to achieve comprehensive three-dimensional visualization of tetrahedral microlattices, enabling detailed analysis of their inner structure at various deformation stages. While traditional techniques such as scanning electron microscopy or helium ion microscopy offer higher resolution, they are limited to external surface visualization. By contrast, nanoCT revealed critical internal features, such as deviations from the CAD model and the presence of random pores and defects in the sample cores (Video S1, 26 s; Fig. S3). These defects, which are undetectable with 2D imaging, were attributed to localized explosions caused by heat accumulation during the printing process.[28]

NanoCT data also provided improved precision in relative density calculations compared to conventional methods, which rely on 2D measurements aligned with the CAD model. For defect-free samples, the relative density derived from nanoCT segmentation was 20.2 ± 0.3%, compared to 17.4% using previous methods. Observed deviations from the CAD model, such as beam buckling and variations in horizontal beam width ($d_{horizontal}$), were attributed to inhomogeneous shrinkage during fabrication [Fig. 1(g, h) and Fig. S1]. These deviations, which were most pronounced in larger planes (planes 2 and 4) containing many thin beams [Fig. S1(a)], corresponded to minor dimensional differences (~600 nm, or ~5 pixels in the nanoCT images), slightly exceeding the spatial resolution. Despite these deviations, uniformity was observed in other planes and inclined beams, as confirmed by thickness mesh analysis [Fig. 1(f), (h); Video S2]. For samples with higher aspect ratios or thinner beams, nanoCT may face challenges due to reduced contrast between structures, emphasizing the need for optimized imaging conditions in such cases.

Local deformation effects in the microlattices were analyzed through manual measurements of plane heights during compression (Fig. 2) and automated image registration of displacement fields [Fig. 3(a)]. Both methods exhibited good agreement, with percentage differences shown in Fig. S6. While percentage errors appeared large, nominal differences were generally below the nanoCT resolution (~300 nm), with a maximum discrepancy of ~600 nm for displacements of ~4 µm. Cross sections during compression [Fig. 2(b)] revealed beam buckling under load, indicating high local stresses in thin beams with negligible nodal contributions.[2,6,10,29] This behavior was more pronounced near defects (Fig. 3), where the absence of counterforce reduced displacement magnitude and led to localized height reductions between planes 3 and 4 [Fig. 2(b)]. These effects were consistently captured by manual measurements, image registration, and FE simulations.

Notably, horizontal slices from simulations and image registration showed that displacement field distortions were confined to beams above the defect (node 0), while neighboring nodes remained relatively unaffected [Fig. 2(b)]. Similar localized effects have been observed in FE simulations of octet-truss structures.[8] These distortions decayed quickly away from the defect, leaving surrounding regions largely unaffected. Additionally, manual measurements in Fig. 2(b) showed greater variation in beam displacements around the nodes at positions +1 and −1 in the defective structure, indicating localized deformation. Node rotation in plane 3 further corroborates these findings (Fig. S7).[30]

Strain analysis in the loading direction (Fig. 4) highlighted the impact of defects. FE simulations showed near-zero strain at the central node of defective samples during steps I and II, compared to −4 and −10% at the same node in defect-free samples. Strain reductions were localized around the defect, with similar strain distributions observed elsewhere in both samples. These findings suggest that defects significantly reduce structural stiffness. This conclusion was supported by reaction force calculations (calculated as the surface integral of stress over the plane 5), where defect-free samples required forces of 58.2 and 115.9 mN for compression steps I and II, compared to 57.0 and 113.7 mN in defective samples, indicating a 2% reduction in stiffness. Experimental forces (8 and 12 mN) were an order of magnitude lower, reflecting significant relaxation processes in the polymeric material, further softening the lattice compared to its linear-elastic counterpart. The extended acquisition

times required for laboratory-based nanoCT scans also influence mechanical deformation behavior, enabling relaxation effects that must be considered when evaluating the properties of polymeric lattice structures. Further studies are needed to assess the impact of radiation on the mechanical performance of these materials.

Comparison with strain maps from image registration (Fig. S5) revealed discrepancies, with experimentally reconstructed maps predicting unrealistically high tensile strains (~30%) at node centers during compression. These errors likely stem from reconstruction limitations at sharp edges between nodes and beams, propagating inaccuracies throughout the strain field.

Conclusions

In summary, the analysis presented here demonstrates the capability of laboratory-based *in situ* nanoCT for investigating the deformation behavior of complex microlattices, capturing local effects around defects with high precision. Using defect-free and defective 3D-printed polymeric microlattices as a case study, comprehensive structural and mechanical characterization at the micrometer scale was demonstrated. NanoCT imaging with a voxel size < 130 nm allowed detailed geometric analysis, while *in situ* loading stages and image registration enabled precise tracking of local displacements and strain distributions. Finite element simulations corroborated experimental findings, confirming the technique's accuracy and highlighting its potential for rational design and optimization of microlattice metamaterials.

Acknowledgments

This work was partly carried out with the support of the Karlsruhe Nano Micro Facility (KNMF, www.knmf.kit.edu), a Helmholtz Research Infrastructure at Karlsruhe Institute of Technology (KIT, www.kit.edu). The Xradia 810 Ultra (nanoCT) core facility was supported (in part) by the 3DMM2O—Cluster of Excellence (EXC-2082/1–390761711). The authors thank Patrick Ziemke for his help in creating the structure in Abaqus/CAE for the FE simulations.

Author contributions

R. Debastiani: Investigation, Formal analysis, Data curation, Validation, Visualization, Writing—original draft (lead), and Writing—review & editing (supporting). C.M. Kurpiers: Investigation, Formal analysis, Validation, and Writing—original draft (lead). S. Gomez Melo and J. Blumberg: Investigation, Formal analysis, Data curation, Software, Validation, Visualization, and Writing—original draft (supporting). U.S. Schwarz and P. Gumbsch: Conceptualization, Methodology, Project administration, Resources, Funding acquisition, Writing—review & editing (supporting), and Supervision. R. Schwaiger: Conceptualization (lead), Methodology, Project administration, Resources, Visualization, Funding acquisition, Writing—review & editing (lead), and Supervision.

Funding

Open Access funding enabled and organized by Projekt DEAL. Funding was provided by Deutsche Forschungsgemeinschaft (DFG), EXC-2082/1–390761711 and EXC-2082/2–390761711.

Data availability

The nanoCT data and the simulation codes are available via Zenodo.org (https://doi.org/10.5281/zenodo.15389357).

Declarations

Competing Interests

The authors declare that they have no known competing financial interests or personal relationships that could have appeared to influence the work reported in this paper.

Open Access

This article is licensed under a Creative Commons Attribution 4.0 International License, which permits use, sharing, adaptation, distribution and reproduction in any medium or format, as long as you give appropriate credit to the original author(s) and the source, provide a link to the Creative Commons licence, and indicate if changes were made. The images or other third party material in this article are included in the article's Creative Commons licence, unless indicated otherwise in a credit line to the material. If material is not included in the article's Creative Commons licence and your intended use is not permitted by statutory regulation or exceeds the permitted use, you will need to obtain permission directly from the copyright holder. To view a copy of this licence, visit http://creativecommons.org/licenses/by/4.0/.

Supplementary Information

The online version contains supplementary material available at https://doi.org/10.1557/s43579-026-01056-0.

References

1. J.U. Surjadi, C.M. Portela, Enabling three-dimensional architected materials across length scales and timescales. Nat. Mater. **24**, 493–505 (2025). https://doi.org/10.1038/s41563-025-02119-8
2. R. Schwaiger, L.R. Meza, X. Li, The extreme mechanics of micro- and nano-architected materials. MRS Bull. **44**, 758–765 (2019). https://doi.org/10.1557/mrs.2019.230
3. S. Banerjee, M.L. Gardel, U.S. Schwarz, The actin cytoskeleton as an active adaptive material. Annu. Rev. Condens. Matter Phys. **11**, 421–439 (2020). https://doi.org/10.1146/annurev-conmatphys-031218-013231
4. J. Bauer, A. Guell Izard, Y. Zhang, T. Baldacchini, L. Valdevit, Programmable mechanical properties of two-photon polymerized materials: from

nanowires to bulk. Adv. Mater. Technol. **4**, 1900146 (2019). https://doi.org/10.1002/admt.201900146
5. C.M. Kurpiers, S. Hengsbach, R. Schwaiger, Architectural tunability of mechanical metamaterials in the nanometer range. MRS Adv. **6**, 507–512 (2021). https://doi.org/10.1557/s43580-021-00094-1
6. C.M. Portela, J.R. Greer, D.M. Kochmann, Impact of node geometry on the effective stiffness of non-slender three-dimensional truss lattice architectures. Extreme Mech. Lett. **22**, 138–148 (2018). https://doi.org/10.1016/j.eml.2018.06.004
7. T. Frenzel, C. Findeisen, M. Kadic, P. Gumbsch, M. Wegener, Tailored buckling microlattices as reusable light-weight shock absorbers. Adv. Mater. **28**, 5865–5870 (2016). https://doi.org/10.1002/adma.201600610
8. Z. Vangelatos, K. Komvopoulos, C.P. Grigoropoulos, Vacancies for controlling the behavior of microstructured three-dimensional mechanical metamaterials. Math. Mech. Solids **24**, 511–524 (2019). https://doi.org/10.1177/1081286518810739
9. A. Gross, P. Pantidis, K. Bertoldi, S. Gerasimidis, Correlation between topology and elastic properties of imperfect truss-lattice materials. J. Mech. Phys. Solids **124**, 577–598 (2019). https://doi.org/10.1016/j.jmps.2018.11.007
10. L.R. Meza, G.P. Phlipot, C.M. Portela, A. Maggi, L.C. Montemayor, A. Comella, D.A. Kochmann, J.R. Greer, Reexamining the mechanical property space of three-dimensional lattice architectures. Acta Mater. **140**, 424–432 (2017). https://doi.org/10.1016/j.actamat.2017.08.052
11. E. Hu, I.P. Seetoh, C.Q. Lai, Machine learning assisted investigation of defect influence on the mechanical properties of additively manufactured architected materials. Int. J. Mech. Sci. **221**, 107190 (2022). https://doi.org/10.1016/j.ijmecsci.2022.107190
12. A. Schroer, J.M. Wheeler, R. Schwaiger, Deformation behavior and energy absorption capability of polymer and ceramic-polymer composite microlattices under cyclic loading. J. Mater. Res. **33**, 274–289 (2018). https://doi.org/10.1557/jmr.2017.485
13. Z. Vangelatos, K. Komvopoulos, C.P. Grigoropoulos, Regulating the mechanical behavior of metamaterial microlattices by tactical structure modification. J. Mech. Phys. Solids **144**, 104112 (2020). https://doi.org/10.1016/j.jmps.2020.104112
14. B.M. Patterson, N.L. Cordes, K. Henderson, J.C.E. Mertens, A.J. Clarke, B. Hornberger, A. Merkle, S. Etchin, A. Tkachuk, M. Leibowitz, D. Trapp, W. Qiu, B. Zhang, H. Bale, X. Lu, R. Hartwell, P.J. Withers, R.S. Bradley, In situ laboratory-based transmission X-ray microscopy and tomography of material deformation at the nanoscale. Exp. Mech. **56**, 1585–1597 (2016). https://doi.org/10.1007/s11340-016-0197-3
15. S.R. Daemi, X. Lu, D. Sykes, J. Behnsen, C. Tan, A. Palacios-Padros, J. Cookson, E. Petrucco, P.J. Withers, D.J.L. Brett, P.R. Shearing, 4D visualisation of in situ nano-compression of Li-ion cathode materials to mimic early stage calendering. Mater. Horiz. **6**, 612–617 (2019). https://doi.org/10.1039/C8MH01533C
16. S. Schäfer, F. Willot, H. Bale, M. Norouzi Rad, S.T. Kelly, D. Enke, Intermittent in-situ high-resolution X-ray microscopy of 400-nm porous glass under uniaxial compression: study of pore changes and crack formation. Scripta Mater. **255**, 116396 (2025). https://doi.org/10.1016/j.scriptamat.2024.116396
17. B.K. Bay, T.S. Smith, D.P. Fyhrie, M. Saad, Digital volume correlation: three-dimensional strain mapping using X-ray tomography. Exp. Mech. **39**, 217–226 (1999). https://doi.org/10.1007/BF02323555
18. F. Gillard, R. Boardman, M. Mavrogordato, D. Hollis, I. Sinclair, F. Pierron, M. Browne, The application of digital volume correlation (DVC) to study the microstructural behaviour of trabecular bone during compression. J. Mech. Behav. Biomed. Mater. **29**, 480–499 (2014). https://doi.org/10.1016/j.jmbbm.2013.09.014
19. W. Hu, X. Cao, X. Zhang, Z. Huang, Z. Chen, W. Wu, L. Xi, Y. Li, D. Fang, Deformation mechanisms and mechanical performances of architected mechanical metamaterials with gyroid topologies: synchrotron X-ray radiation in-situ compression experiments and 3D image based finite element analysis. Extreme Mech. Lett. **44**, 101229 (2021). https://doi.org/10.1016/j.eml.2021.101229
20. W. Wu, D. Qi, W. Hu, L. Xi, L. Sun, B. Liao, F. Berto, G. Qian, D. Xiao, Synchrotron X-ray micro-computed tomography imaging of 3D re-entrant micro lattice during in situ micro compression experimental process. Mater. Des. **192**, 108743 (2020). https://doi.org/10.1016/j.matdes.2020.108743
21. M. Valmalle, B. Smaniotto, J. Lian, L. St-Pierre, F. Hild, On the evaluation of in-situ mechanical properties of an additively manufactured BCC lattice. Mech. Mater. **215**, 105602 (2026). https://doi.org/10.1016/j.mechmat.2026.105602
22. R. Debastiani, C.M. Kurpiers, E.D. Lemma, B. Breitung, M. Bastmeyer, R. Schwaiger, P. Gumbsch, Dealing with missing angular sections in NanoCT reconstructions of low contrast polymeric samples employing a mechanical in situ loading stage. Microsc. Res. Tech. **88**, 832–838 (2025). https://doi.org/10.1002/jemt.24746
23. S. Klein, M. Staring, K. Murphy, M.A. Viergever, J.P.W. Pluim, elastix: a toolbox for intensity-based medical image registration. IEEE Trans. Med. Imaging **29**, 196–205 (2010). https://doi.org/10.1109/tmi.2009.2035616
24. J.W. Blumberg, U.S. Schwarz, Comparison of direct and inverse methods for 2.5D traction force microscopy. PLoS One **17**, e0262773 (2022). https://doi.org/10.1371/journal.pone.0262773
25. M. Alnæs, J. Blechta, J. Hake, A. Johansson, B. Kehlet, A. Logg, C. Richardson, J. Ring, M.E. Rognes, G.N. Wells, The FEniCS project version 1.5. Arch. Numer. Softw. 3 (2015). https://doi.org/10.11588/ans.2015.100.20553
26. C. Geuzaine, J.-F. Remacle, Gmsh: a 3-D finite element mesh generator with built-in pre- and post-processing facilities. Int. J. Numer. Methods Eng. **79**, 1309–1331 (2009). https://doi.org/10.1002/nme.2579
27. C.M. Kurpiers, Untersuchung der Mikrostruktureinflüsse auf die mechanischen Eigenschaften von Nano- und Mikroarchitekturen (Dissertation, KIT-Bibliothek, Karlsruhe, 2024). https://doi.org/10.5445/ir/1000166935
28. J.B. Mueller, J. Fischer, Y.J. Mange, T. Nann, M. Wegener, In-situ local temperature measurement during three-dimensional direct laser writing. Appl. Phys. Lett. **103**, 123107 (2013). https://doi.org/10.1063/1.4821556
29. X. Zhang, A. Vyatskikh, H. Gao, J.R. Greer, X. Li, Lightweight, flaw-tolerant, and ultrastrong nanoarchitected carbon. Proc. Natl. Acad. Sci. USA **116**, 6665–6672 (2019). https://doi.org/10.1073/pnas.1817309116
30. J.G. Meijer, F.H. Shaik, V.V. McDermott, H.M. Jaeger, Diffusive buckling fronts in lattice-based metamaterials. PNAS Nexus **5**, pgag272 (2026). https://doi.org/10.1093/pnasnexus/pgag272

Publisher's Note Springer Nature remains neutral with regard to jurisdictional claims in published maps and institutional affiliations.